



OPEN

A fast methodology for generating skeletal FEM with detailed human geometric features based on CPD and RBF algorithms

Qiuqi Yuan¹, Binhui Jiang¹✉, Xiaoming Zhu², Jingzhou Hu³, Yulong Wang⁴, Clifford C. Chou⁵ & Shiwei Xu¹✉

Due to the significant effects of the human anatomical characteristics on the injury mechanism of passenger in traffic accidents, it is necessary to develop human body FEM (Finite Element Model) with detailed anatomical characteristics. However, traditional development of a human body FEM is an extremely complicated process. In particular, the meshing of human body is a huge and time-consuming project. In this paper, a new fast methodology based on CPD (Coherent Point Drift) and RBF (Radial Basis Function) was proposed to achieve the rapid developing the FEM of human bone with detailed anatomical characteristics. In this methodology, the mesh morphing technology based the RBF was used to generate FEM mesh in the geometry extracted from the target CT (Computed Tomography) data. In order to further improve the accuracy and speed of mesh morphing, the target geometric feature points required in the mesh morphing process were realized via the rapid and automatic generation based on the point-cloud registration technology of the CPD algorithm. Finally, this new methodology was used to generate a 3-year-old ribcage FEM consisting of a total of 27,728 elements with mesh size 3–5 mm based on the THUMS (Total Human Model for Safety) adult model. In the entire process of generating this new ribcage model, it only took about 2.7 s. The average error between the new FEM and target geometries was only about 2.7 mm. This indicated that the new FEM well described the detailed anatomical characteristics of target geometry, thus importantly revealing that the mesh quality of the new FEM was basically similar to that of source FEM.

Passenger injury caused by traffic accidents is a serious public health issue worldwide^{1,2}. Injury mechanism of passenger resulting from different traffic accidents plays an important role in the theoretical basis for solving such public health issue. It has been demonstrated that the human anatomical characteristics have significantly effects on the injury mechanism of passenger³. For example, Ridella et al.⁴ reported that obese elderly and child passengers were more likely to be injured than those with normal body characteristics. Therefore, it is greatly significant to study the influences of human anatomical characteristics on injury mechanisms towards the protection of special passengers.

As of today, computational simulation has become one of the main methods to study injury mechanism and establish injury tolerances⁵. In particular, the detailed biomechanical responses of human tissue pertaining to injury severity and location, such as strain and stress, can be predicted by the human body FEM (finite element model). In addition, the human body FEM can accurately characterize the anatomical features of human body. The human body FEM has become one of the most widely used human injury assessment tool in the field of vehicle safety⁶. Therefore, numerous human body FEMs, including the H (Human) model, FHBM (Ford Human Body Model), THUMS (Total Human Model for Safety), GHBM (Global Human Body Model Consortium) et al., have been developed^{7–10}. The process of development for a human body FEM is very complicated and

¹State Key Laboratory of Advanced Design and Manufacturing for Vehicle Body, Hunan University, Changsha 410082, People's Republic of China. ²Shanghai Motor Vehicle Inspection Certification and Tech Innovation Center Co., Ltd., Shanghai 201805, People's Republic of China. ³Department of Oral and Maxillofacial-Head and Neck Oncology, Shanghai Ninth People's Hospital, Shanghai Jiao Tong University School of Medicine, Shanghai 200023, People's Republic of China. ⁴Auto Engineering Research Institute, Guangzhou Automobile Group Co., Ltd., Guangzhou 511434, People's Republic of China. ⁵Bioengineering Center, Wayne State University, Detroit, MI 48201, USA. ✉email: jjhhzz123@163.com; xushiwei@hnu.edu.cn

usually includes: 1. creation of human body geometric model from CT (Computed tomography) and MRI (Magnetic resonance imaging) data, 2. FE meshing of human body geometric model, and 3. boundaries, loading, and verification of model. One of the most time-consuming is the meshing process of the geometric model. Existing meshing methods mainly include Delaunay, Advancing Front Technique, Mapping, Sweeping^{11,12}. In practical use, the geometric model is decomposed and the meshes are generated mainly through manual interaction. However, for the human body structure with very complex geometric details, the mesh generated by the above methods is of poor quality and can hardly meet the analysis requirements. It requires experienced researchers to improve mesh quality by Laplacian smoothing, elements topology optimization and other operations^{13,14}.

Due to the complexity of human body FEM development, the method to obtain new FEM based on the existing basic model through mesh deformation technology has been widely developed. The scaling method was firstly proposed. For example, Vavalle et al.¹⁵ and Schoell et al.¹⁶ scaled the 50th male FEM in the GHBMC to obtain a 95th adult male and a 65-year-old male FEM, respectively. In the scaling method, the new FEM is usually obtained by scaling the body parts of the existing basic FEM with different ratios without need of the detailed geometric data of the target geometry. This advantage makes the scaling method widely used in literatures^{17–19}. However, the disadvantage of the scaling method is also obvious in aspect that the detailed geometric differences between the body parts of the target FEM and the existing basic FEM are not reflected. Considering this disadvantage of the scaling method, the UMTRI (University of Michigan Transportation Research Institute) and Hunan University recently proposed a mesh morphing method based on feature points and RBF (Radial Basis Functions)^{20–23}. Mesh morphing is the smooth transition of a FEM into another similar FEM, where the first model is called the source FEM and the second is called the target FEM. Mesh morphing usually consists of three steps: Firstly, a large number of corresponding feature points are selected at appropriate locations of source FEM and target geometry. Then, the corresponding relationship between them is established through feature points, such as the corresponding relationship between vertices, edges and surfaces. Finally, the meshes of source FEM are mapped to the target geometry by RBF, so the target FEM is obtained. The target FEM generated by mesh morphing can retain the detailed geometric features of target geometry well. However, the limitation of mesh morphing is that a large number of feature points need to be selected manually, which is very time-consuming and laborious. For example, using mesh morphing to generate a ribcage FEM with 27,728 elements usually needs to manually select more than 1,000 feature points²⁴. Moreover, once the sequence and number of feature points on the source FEM and the target geometry are inconsistent, the process of mesh morphing cannot be carried out. Considering all of these is necessary to improve such a time-consuming, labor-intensive, and error-prone step.

In this paper, in order to avoid the disadvantage of the mesh morphing method, an automatic generating feature points method using the CPD (Coherent Point Drift) algorithm was proposed. This new methodology was then applied to automatically generate feature points for different human bones, such as ribcage, pelvis, humerus, radius, tibia, and ulna. Furthermore, using the generated feature points, the FE meshing of these human bones was generated by the mesh morphing with RBF. In these applications, generating about 200 and 2000 feature points only takes about 2 s and 24 s, respectively. The quality of FE mesh obtained by using the automatically generating feature points is basically the same as that of FE mesh prior to the morphing. Results reveal that this method capable of generating the feature points automatically is faster and more accurate than the manual extraction.

Method

The Ethical Committee of Shanghai Ninth People's Hospital approved this retrospective study. And written informed consent was obtained from all the participants. All methods were performed in accordance with relevant named guidelines and regulations.

A whole process from CT data to the FEM using the fast mesh morphing method is shown in Fig. 1. First of all, the geometry of target new model described by point-cloud was extracted from CT data (ribcage, pelvis, humerus, radius, tibia and ulna). In this process, the ribcage was taken as an example of the target new model. Second, the corresponding source FEM of ribcage was split from THUMS, and outermost mesh nodes were extracted as the source point-cloud. Third, a rough registration between the target and source point-clouds was conducted through PCA (Principal Component Analysis) with CPD algorithm to obtain feature points. Finally, the feature points were used to morph the source FEM for target FEM.

The geometry of target new model. In this study, a CT data of the whole-body for a 3-year-old male child was used to develop the target shape. By adjusting the CT value, the data related to the bone was extracted. Then, the data of bone was thresholding, and smoothed. Sometimes, the CT image quality is not good enough to capture all the geometrical details. For this, threshold adjustment was used to improve the completeness of the geometry. The target shape was then repaired by editing mask. Generally speaking, the complete usable shape mask can be extracted through the preprocessing process described above. The pre-processing process is shown in Fig. 2. The data processed above were exported in the form of a point-cloud.

The source FEM. The skeletal FEMs were split from THUMS and marked as FEM_S for source FEMs. Then the outermost nodes of each FEM_S were extracted as the source point-cloud for each bone and marked as P_S .

Automatically generating feature points. Figure 3 shows the method overview for automatically generating feature points. Firstly, the target point-cloud extracted from CT data was filtered. Then the coordinate system of target point-cloud and source point-cloud was unified through rough registration. Finally, non-rigid registration was carried out from source point-cloud to target point-cloud to obtain target feature points based on CPD algorithm.

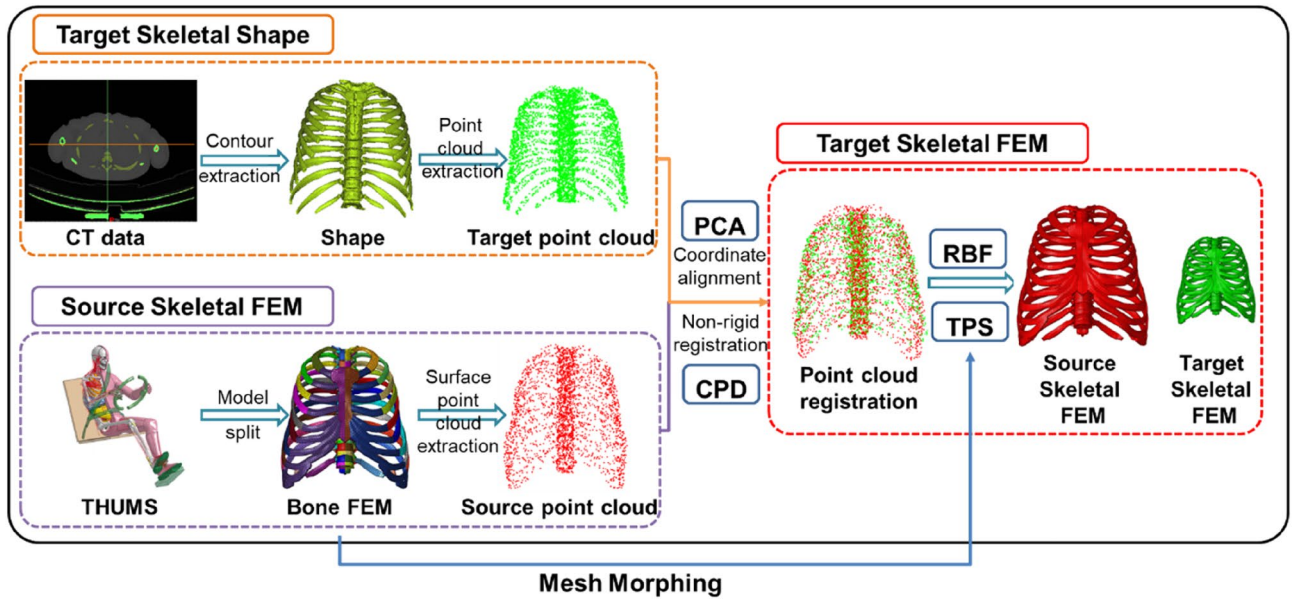


Figure 1. Overview of the fast mesh morphing method.

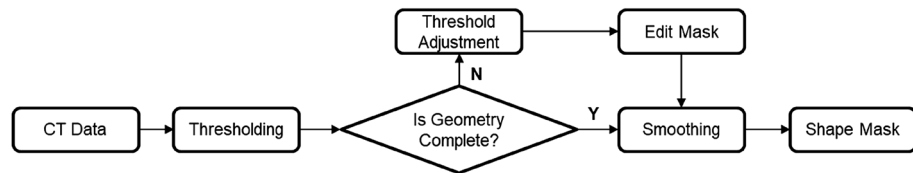


Figure 2. Flow chart of preprocessing part of CT data.

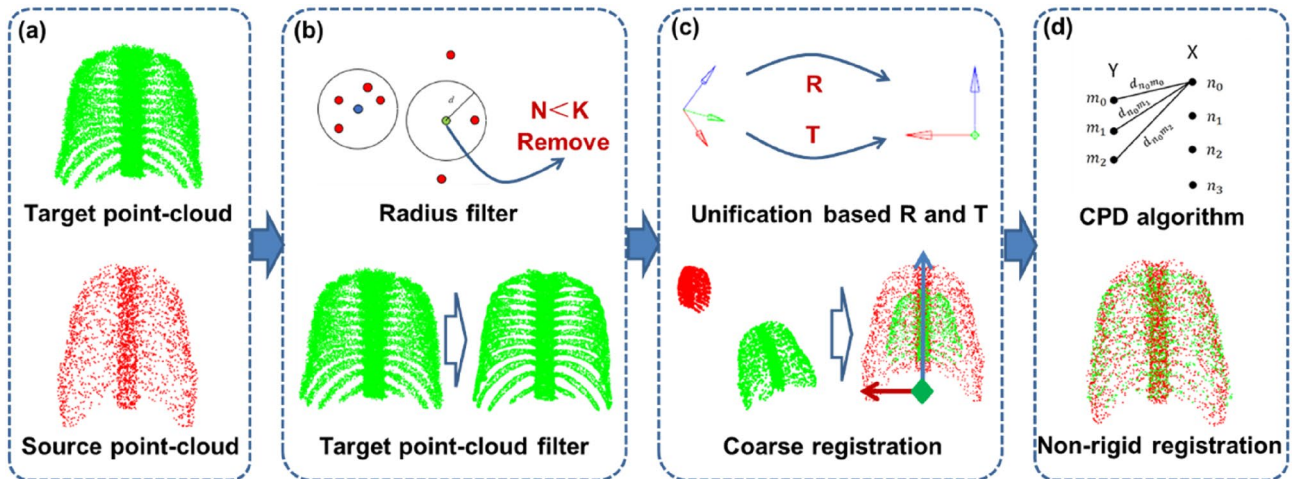


Figure 3. Method overview for generating feature points. (a) Point-cloud set; (b) Point-cloud filter; (c) Coordinate system unification; (d) Non-rigid registration.

Radius filtering of point-clouds. When the point-cloud of target shape was generated from CT data, it usually had a large number of points with outliers (i.e., noise points) in Fig. 3a. These noise points may cause the mismatches during the registration of the target and source point-clouds. Therefore, the radius filter was adopted to remove these noise points. In the area with a point as the center and d as the radius, if the number of points is less than K , the center point will be removed by the radius filter. In this study, the radius d and the number of points K was defined as 2 mm and 5, respectively. As shown in Fig. 3b, the noise points in the point-cloud of target shape were significantly reduced by the radius filter. The point-cloud of target shape without noise points was marked as $P_{C,I}$.

Coordinate system unification. Usually, there is a huge difference of spatial position between P_{C_I} and P_S , because these two point-clouds were obtained in different coordinate systems. Therefore, it is necessary to unify the coordinate systems of these two point-clouds through matrix operations in Eq. (1).

$$P_C = P_{C_I} * R_0 + T_0 \quad (1)$$

where P_C is the transformed point-cloud of P_{C_I} in the coordinate system of P_S ; R_0 is rotation matrix; T_0 is translation matrix.

Using Eq. (1), the difficult step is to find out the rotation and translation matrices. Considering this, the PCA-based coarse registration method was adopted in this study, as shown in Fig. 3c²⁵. In the PCA-based coarse registration, principal component analysis was used to reveal the main distribution direction of point-cloud and reduce dimension of the data. Therefore, the PCA-based coarse registration method is mainly based on the global principal axis direction of point-cloud data for registration. Firstly, the covariance matrix of P_{C_I} and P_S was calculated. And then, the main feature component, namely the global principal axis direction of the point-cloud data, was calculated according to the covariance matrix to make up the principal axis direction matrices. So, R_0 can be obtained by the principal axis direction matrices by Eq. (2). Finally, the coordinate values of center point calculated from two point-clouds and rotation matrix R_0 were used to obtain the translation matrix T_0 using Eq. (3).

$$R_0 = U_P U_X^{-1} \quad (2)$$

$$T_0 = \overline{P_S} - R_0 * \overline{P_{C_I}} \quad (3)$$

where U_X and U_P are the 3*3 principal axis direction matrices of point-clouds P_S and P_{C_I} , respectively; $\overline{P_S}$ and $\overline{P_{C_I}}$ are the coordinate values of center point of point-clouds P_S and P_{C_I} , respectively.

Non-rigid registration. The P_C and P_S were aligned on the principal axis directions after the Coordinate System Unification. However, the mesh morphing technology is based on the same number of source and target feature points to achieve element mapping transformation. Hence it is necessary to create an equal number of source and target feature points in P_C and P_S . Considering the P_S as extracted from the outermost nodes of the FEM with high quality mesh, therefore, the P_S can be directly used as the source feature points. For the target feature points, a non-rigid registration was adapted to mapping the source feature points to the P_C . The target feature points generated by this method not only can be consistent with the source feature points in number, but also have a similar distribution position in human body geometry to the source feature points. This can effectively reduce the distortion of the generating element in the mesh morphing. This non-rigid registration named as alignment depicted in Fig. 3d was realized by the CPD algorithm²⁶.

The essence of obtaining target feature points by the non-rigid registration based on the CPD algorithm is to find out an accurate transformation matrix marked as T. Using this accurate T to transform P_S can obtain a new point set P_{c_c} which deems to be as similar as possible to point-cloud P_C . P_{c_c} can be used as the target feature points in the mesh morphing technology. In order to obtain an accurate T, the Gaussian Mixture Model (GMM) was adapted to address this problem in CPD algorithm. In the GMM, P_S was considered as the GMM centroids and P_C was considered as the GMM generated point-cloud. In other words, P_S was regarded as a correct standard point-cloud, and P_C was the point-cloud composed of many scattered points around P_S . The relationship set between P_S and P_C in the GMM can be expressed by Eqs. (4) and (5). From Eq. (4), it can be found that the probability of the existence of a point in P_C was described as the sum of the distance between this point and each GMM centroid (each point in P_S). Since P_{c_c} obtained by transformation of P_S through the accurate T was as completely coincident with P_C as possible. It should also be pointed out that there is always a point in P_{c_c} that can coincide with the corresponding point in P_C (the distance between these two points is zero). Therefore, different T can be tried repeatedly to transform P_S to obtain different P_{c_c} . The possibility of all point in each P_{c_c} was summed up by Eq. (6). This cumulative sum obtained by Eq. (6) can be used as the rating of the different T: the greater of the cumulative sum implies the higher score and more accurate of T. Accordingly, finding the accurate T needs to calculate the maximum value of the function described by Eq. (6). By maximizing the likelihood function described in Eq. (6), the parameters (θ and σ^2) in T can be obtained. Finally, P_{c_c} were calculated from transformation of P_S by T.

$$p(P_C) = w \frac{1}{N} + (1 - w) \sum_{m=1}^M \frac{1}{M} p(P_C|m) \quad (4)$$

where $p(P_C)$ is represented as the generation probability of each point in P_C ; N is the number of points in P_C ; M is the number of points in P_S , and w is the weight factor; $p(P_C|m)$ is the probability of the points in P_C generated by each point in P_S and can be calculated by Eq. (5).

$$p(P_C|m) = \frac{1}{(2\pi\sigma^2)^{D/2}} \exp^{-\frac{x-y_m^2}{2\sigma^2}} \quad (5)$$

$$E(\theta, \sigma^2) = - \sum_{n=1}^N \log \sum_{m=1}^{M+1} P(m) p(X|m) \quad (6)$$

where θ is the parameter set consisting of the rotation matrix R , translation matrix T , and deformation matrix X ; Y_m is the center of GMM model; X is the points generated by the GMM model; D is the dimensions of points in P_C and P_S .

Mesh morphing technology. After the alignment of P_C and P_S in Section "Non-rigid registration", the outermost nodes (point-cloud P_S) in the source FEM were already mapped to the target shape described by P_C . If the internal nodes in the source FEM can be mapped regularly into the target shape as expressed in Eq. (7), implying that target FEM with detailed target geometric characteristics will be obtained. This method for obtaining a new FEM is called as the mesh morphing technology. In 2016, Wang et al.²⁴ firstly proposed a mesh morphing technology based on RBF with kernel function TPS (Thin Plate Spline)²⁷ expressed as given in Eq. (8). In the RBF with kernel function TPS as given in Eq. (9), the source and target feature points obtained in Section "Automatically generating feature points" was used as the control points to calculate the weight coefficients in Eq. (8) by Eq. (10), then the internal element nodes associated with control points are smoothly transformed from the source FEM to the target FEM by Eq. (7).

$$x_n^{(T)}, y_n^{(T)}, z_n^{(T)} = f(x_n^{(S)}, y_n^{(S)}, z_n^{(S)}) \quad (7)$$

where $f(x, y, z)$ is the transformation function for mapping the internal nodes in the source FEM into the geometry of target new model; $x_n^{(S)}, y_n^{(S)}, z_n^{(S)}$ is the coordinate values of n node in the source FEM; $x_n^{(T)}, y_n^{(T)}, z_n^{(T)}$ is the coordinate values of the corresponding n node in the new target FEM.

$$f(x, y, z) = p(x, y, z) + \sum_{i=1}^h w_i \varnothing \left(\left\| (x, y, z) - \left(x_i^{(S^*)}, y_i^{(S^*)}, z_i^{(S^*)} \right) \right\| \right) \quad (8)$$

where $p(x, y, z)$ is a low order polynomial; \varnothing is the kernel function representing the TPS in this paper; w_i is the weight coefficient, $x_i^{(S^*)}, y_i^{(S^*)}, z_i^{(S^*)}$ is the coordinate values of i node in source feature points; h is representing the number of source feature points.

$$\varnothing = (x, y, z) - \left(x_i^{(S^*)}, y_i^{(S^*)}, z_i^{(S^*)} \right)^2 \log \left(\left\| (x, y, z) - \left(x_i^{(S^*)}, y_i^{(S^*)}, z_i^{(S^*)} \right) \right\| \right) \quad (9)$$

$$\begin{bmatrix} W \\ A \end{bmatrix} = \begin{bmatrix} K & Q \\ Q^T & O \end{bmatrix}^{-1} \begin{bmatrix} V \\ O \end{bmatrix} \quad (10)$$

where $W = [w_1, w_2, w_3, \dots, w_h]$; Q is represented the coordinate values of the source feature points; V is represented as the coordinate values of the target feature points; $A = [a_0, a_x, a_y, a_z]$; K is the distance between each source and its corresponding target feature point.

Results

In order to verify the method proposed in Section "Method", six skeletal FEMs separated from the adult 50th THUMS including ribcage, pelvis, humerus, radius, tibia, and ulna were successfully morphed into the corresponding target shape extracted from a 3-year-old male child CT data as shown in Table 1. Ribcage, pelvis, humerus, radius, tibia, and ulna FEMs generation required 2.7 s, 1.51 s, 0.932 s, 0.85 s, 0.793 s, and 0.73 s, respectively.

Geometric error between target shape and FEM. The distance between the outermost mesh nodes of target FEM and corresponding points of target point-cloud was used to evaluate the geometric error between target shape and FEM as shown in Fig. 4. It can be found that the average geometric error of each model is less than 3 mm, and particularly the average geometric errors of the humerus, radius, tibia and ulna model are less than 1.5 mm. Even the maximum geometric errors of the humerus, radius, tibia and ulna model are less than 5 mm. However, the maximum geometric errors of ribcage and pelvis FEMs are 15.332 and 14.645 mm, respectively. This is mainly due to the filtering of ribcage and pelvis original target point-clouds. The geometric features of ribcage and pelvis are complex, especially their original target point-clouds extracted from CT exhibits a large number of detailed geometric features, thus easily leading to incorrect point-cloud registration. Therefore, their original point-clouds are filtered to reduce useless detailed geometric features. However, the geometric error is the comparison between the target FEM and the original target point-cloud, showing some parts with detailed geometric features are relatively large.

Mesh quality. The mesh quality of solid elements in target FEMs including Jacobian, Warpage, Skew, Aspect ratio et al. were checked and listed in Table 2, showing that the overall mesh quality of the target FEMs was good and basically meets the requirements of finite element analysis. It was generally considered acceptable if the minimum Jacobian of the mesh is ≥ 0.2 . However, it should be noted that the mesh quality of solid elements in target FEMs was a slightly inferior than that of solid elements in source FEMs. For example, compared to the source FEMs, the minimum Jacobians of the target humerus and ulna models were decreased from 0.39 and 0.31 to 0.25 and 0.22, respectively. Because the target feature points generated in Section "Mesh morphing technology" described the detailed geometric features of the target shape as much as possible, this led to a less uniformity of the elements distribution with these target feature points as the outermost nodes and the poor element quality. The mesh quality degraded by this factor can be improved with mesh smoothing.

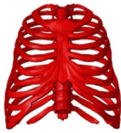

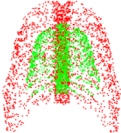
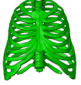
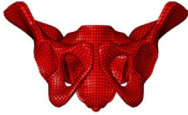

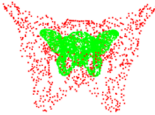



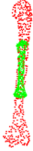













Item	Source FEM	Target geometry data	Source and target feature points	Target FEM
ribcage				
pelvis				
humerus				
radius				
tibia				
ulna				

Table 1. Summary of source and target FEMs.

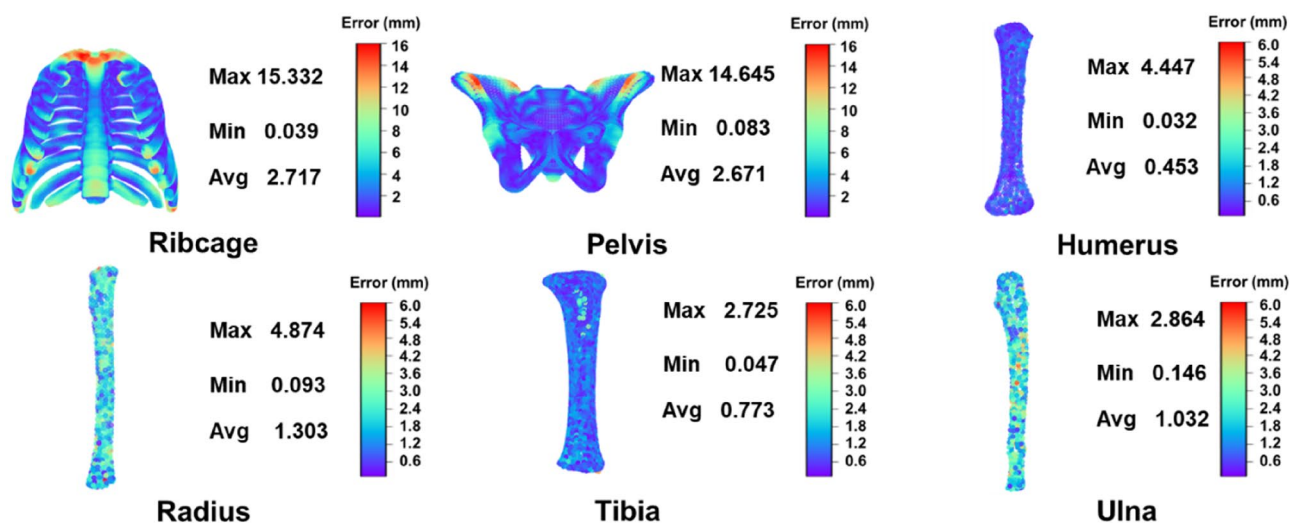


Figure 4. The geometric errors contour of target FEMs.

Item	Jacobian		Warpage		Skew		Aspect ratio		Quad faces minimum angel		Quad faces maximum angel	
	≥ 0.5	Minimum	≤ 30	Maximum	≤ 60	Maximum	≤ 8	Maximum	≥ 30	Minimum	≤ 150	Maximum
Target FEMs												
ribcage	99%	0.41	99%	49	99%	57	99%	4	99%	32	99%	153
pelvis	99%	0.9	99%	48	99%	69	99%	4	97%	14	98%	144
humerus	92%	0.25	90%	65	95%	80	94%	15	90%	16	93%	169
radius	96%	0.34	94%	66	96%	70	93%	11	90%	10	90%	159
tibia	90%	0.24	95%	69	95%	86	97%	6	92%	13	92%	170
ulna	82%	0.22	92%	53	97%	71	96%	5	90%	19	88%	185
Source FEMs												
ribcage	99%	0.41	99%	48	99%	57	99%	4	99%	33	99%	154
pelvis	99%	1	99%	48	99%	67	99%	3	98%	15	99%	138
humerus	97%	0.39	95%	49	99%	46	99%	5	99%	33	98%	157
radius	99%	0.39	95%	47	99%	51	99%	5	98%	22	96%	164
tibia	97%	0.32	96%	49	99%	59	99%	5	99%	22	96%	167
ulna	89%	0.31	99%	58	99%	58	99%	5	97%	22	92%	170

Table 2. Mesh quality of solid elements in target FEMs.

Discussion

In the process of mesh morphing, it was found that the target feature points have significant influences on target FEMs. In this section, the influences of the generation methods and number of target feature points on the geometric error and mesh quality of target FEMs will be discussed.

The influences of generation method of feature points. In this study, the non-rigid registration based on the CPD algorithm was adapted in Section "Automatically generating feature points" to obtain the target feature points. In the non-rigid registration, using coordinate translation, rotation, scaling and local deformation to generate target feature points from source feature points can better describe the geometric characteristics of the target point-cloud. In fact, the target feature points can also be obtained by rigid registration. For CPD algorithm, rigid registration is a transformation that does not change the relative position between two points in the point-cloud, including translation, rotation and scaling. Non-rigid registration can change the relative position between two points in the point-cloud. It can cause local deformation by nonlinear matrix. We did both registrations by changing the θ in Eq. (6). The θ in rigid registration include rotation matrix R , translation matrix T and scaling matrix S . Instead of rigid registration, the θ contains an additional nonlinear matrix N .

As shown in Fig. 5, when using non-rigid registration, ribcage, pelvis, humerus, radius, tibia, and ulna FEMs generation required 44.61 s, 21.9 s, 8.192 s, 5.581 s, 5.988 s, and 4.933 s respectively. However, due to the rigid

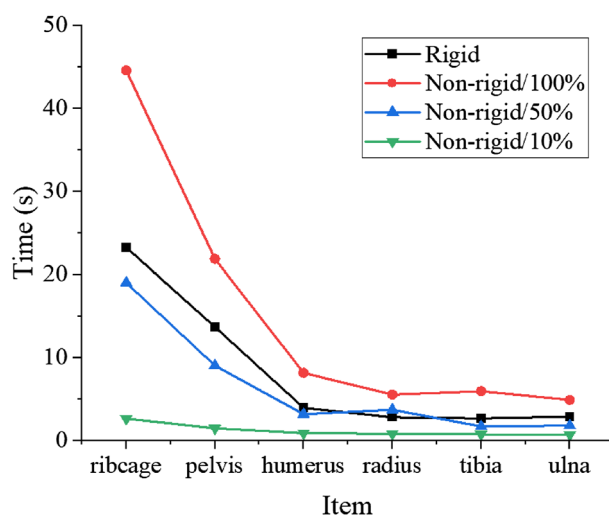


Figure 5. Comparison of the generation time of different bone FEMs under different generation methods and number of feature points.

registration ignores the nonlinear transformation, the FEMs generation time reduced to 23.285 s, 13.724 s, 3.972 s, 2.846 s, 2.714 s, 2.911 s respectively.

In Fig. 6, the geometric errors including maximum and average errors of target FEMs generated by the non-rigid registration method are lower than that generated by the rigid registration. This is mainly because the non-linear transformation is not adapted to make the target feature points closer to the geometric features of the target shape in the rigid registration method. Especially for humerus, radius, tibia, and ulna, their detailed geometric characteristics of source and target point-clouds differ greatly. Therefore, compared with target FEMs generated by the rigid registration, the average geometric error of target FEMs generated by the non-rigid registration are decreased by 73.3%, 72.2%, 77.7% and 66.5%, respectively.

Figure 7 shows that the mesh quality of target FEMs generated by rigid registration are similar to that of source FEMs shown in Table 2. This is mainly because the translation, rotation and scaling in the rigid registration did not cause local deformation of the mesh elements to affect the mesh quality of target FEMs. Therefore, the mesh quality of target FEMs generated by rigid registration were also higher than those of the corresponding target FEMs generated by non-rigid registration.

The influences of number of target feature points. Different number of target feature points have different functional capability to describe the geometric features of target point-cloud, affecting the generation of nodes for the target FEMs in the mesh morphing process. Therefore, the influences of number of target feature points were described in this section. Selecting 100%, 50%, and 10% of source features points by the uniform sampling method were respectively used to generate the corresponding number of target feature points by non-rigid registration for further generating target FEMs. It can be seen from Fig. 5, as the number of feature points decreases, the generation time of target FEMs decreases gradually. When 10% of source features points are selected, the ribcage FEM with 27,728 elements needs only 2.7 s.

Figure 8 shows the geometric errors including the maximum and average errors of target FEMs increased with decreasing of the number of target feature points. The influences of number of target feature points on the geometric errors are slightly in the target FEMs of ribcage and pelvis, but significantly in the target FEMs of humerus, radius, tibia, and ulna. This is primarily due to the detailed geometric characteristics of their source and target point-clouds differ significantly. Therefore, more target feature points are necessary to describe the detailed geometric characteristics of target point-clouds.

Data shown in Table 3, reveal the mesh quality of the target FEMs generated by the small number of target feature points is better. This is mainly due to fewer target feature points that ignore some detailed geometric features of the target point-cloud to reduce the local deformation of mesh elements. Similarly, in the general mesh generation, it is also important and necessary to balance the mesh quality and the details of geometric features.

Limitations. Through presentation and discussion of the method proposed in this study, the source FEMs can be quickly morphed to the target FEMs more consistent with the geometric features of the target point-cloud. However, in order to describe more detailed geometric feature of target point-cloud, a non-rigid registration method is used to locally deform the source feature points to generate target feature points. This local deformation caused a decrease in the mesh quality of the target FEM compared to that of the corresponding source FEM. Especially when the detailed geometric features of the source and target point-clouds differ significantly, the mesh quality of the generated target FEMs decreases more significantly. For the meshes with acceptable quality, we usually improve them by smoothing, elements optimization, nodes optimization and so on. Therefore, it is necessary to conduct more in-depth study on how to balance the mesh quality and the details of geometric

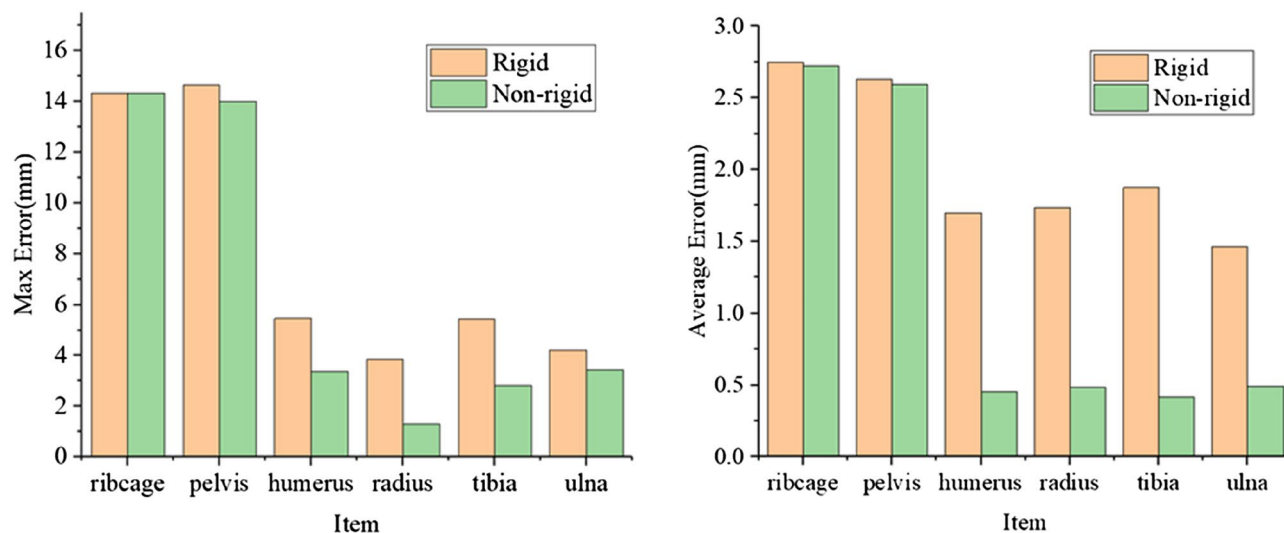


Figure 6. The comparison of geometric errors of target FEMs generated by rigid and non-rigid registration.

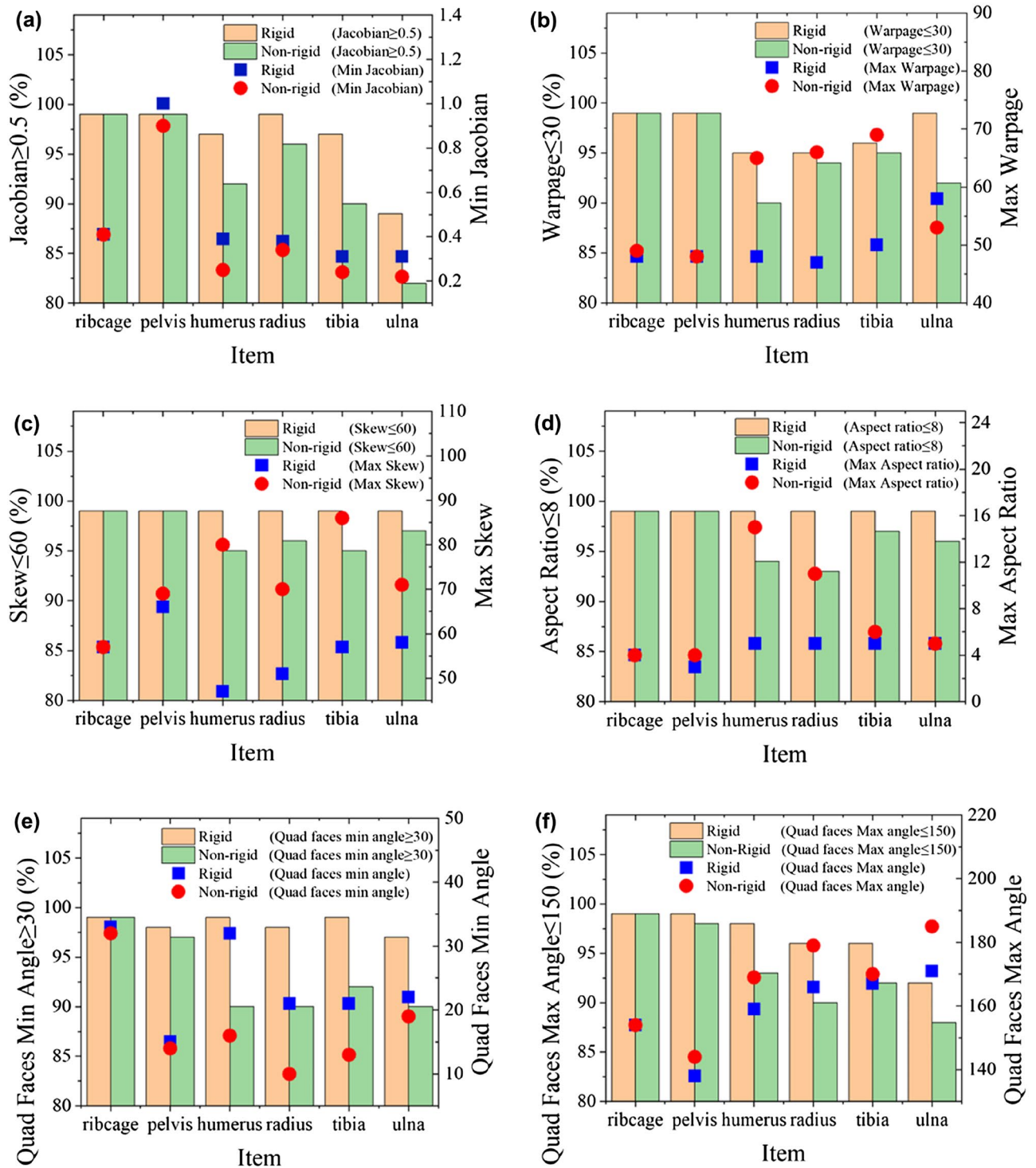


Figure 7. Comparisons of mesh quality of the corresponding target FEMs generated by rigid and non-rigid registration method. (a) Jacobian; (b) Warpage; (c) Skew; (d) Aspect Ratio; (e) Quad faces Min Angle; (f) Quad faces Max Angle.

features of the target point-cloud. In addition, only the human skeletal FEMs were considered in this study, the whole human body FEM also needs to be investigated in future research studies.

Conclusion

In this study, a fast-morphing methodology for generating human skeletal FEM with detailed geometric features based on CPD and RBF algorithms was proposed. This is indeed to be the first time that the CPD algorithm is applied to the traditional mesh morphing technology. Using this algorithm enables realization of the

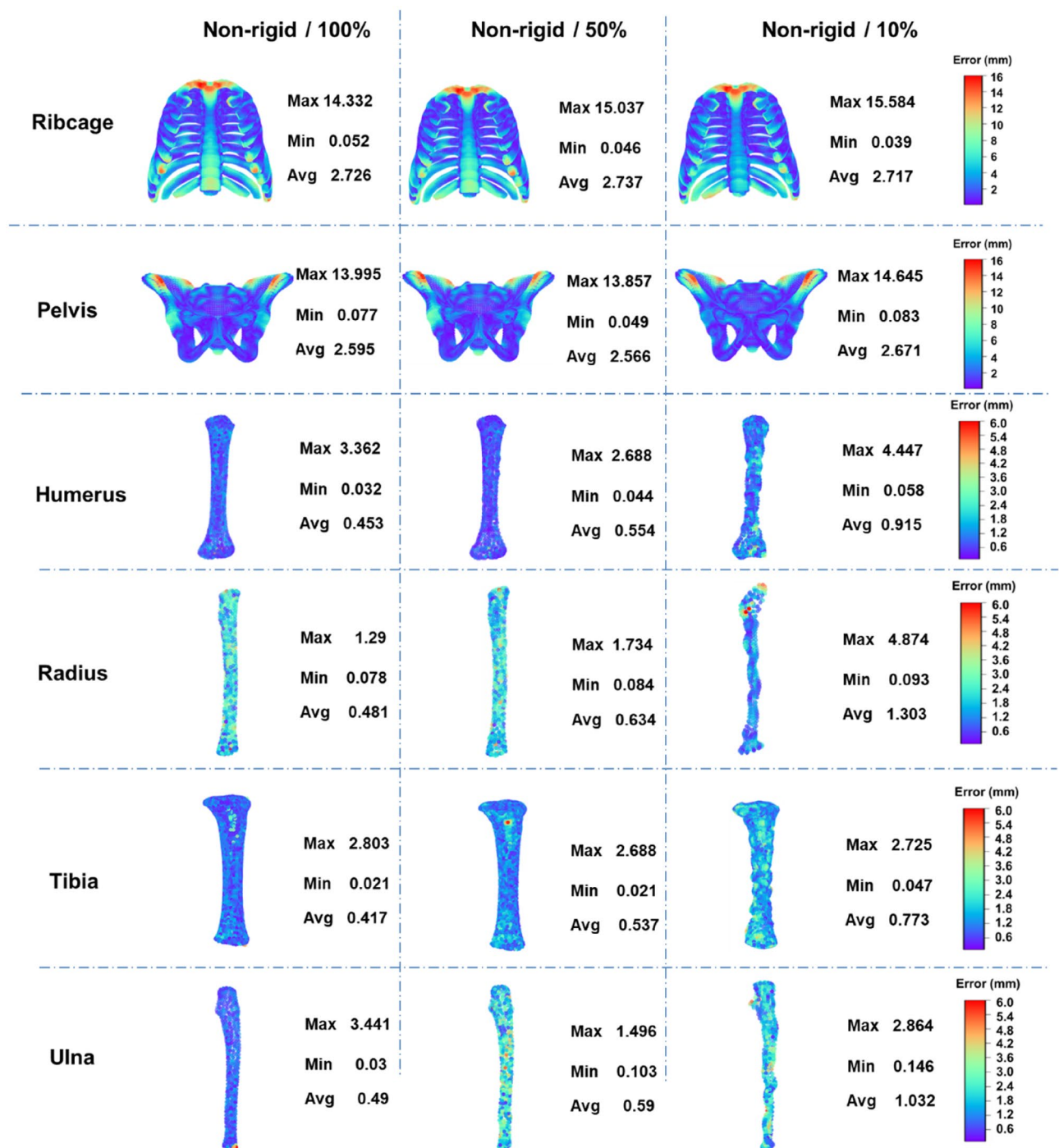


Figure 8. Geometric errors of target finite element model generated with different number of feature points.

improvement from manually placing feature points to automatically generating feature points. In addition, this method can directly use the point-cloud of the target geometric data for finite element modeling to save a lot of work on the reverse modeling. This fast-morphing methodology was successfully used to morph several human skeletal FEMs extracted from THUMS adult model to 3-year-old child skeletal FEMs. The morphing results proved that the human skeletal FEMs generated by this fast-morphing methodology has resulted in small geometric errors and high mesh quality. Limitations on this approach will be continued to be investigated further in research pertaining to this area in the future.

Item	Jacobian		Warpage		Skew			Aspect ratio		Quad faces minimum angel		Quad faces maximum angel
	≥ 0.5	Minimum	≤ 30	Maximum	≤ 60	Maximum	≤ 8	Maximum	≥ 30	Minimum	≤ 150	Maximum
10%												
ribcage	99%	0.41	99%	49	99%	57	99%	4	99%	32	99%	153
pelvis	99%	0.8	99%	48	99%	69	99%	4	97%	14	98%	144
humerus	92%	0.25	90%	65	95%	80	94%	15	90%	16	93%	169
radius	96%	0.34	94%	66	96%	70	93%	11	90%	10	90%	159
tibia	90%	0.24	95%	69	95%	86	97%	6	92%	13	92%	170
ulna	82%	0.22	92%	53	97%	71	96%	5	90%	19	88%	185
50%												
ribcage	99%	0.41	99%	50	99%	57	99%	4	99%	32	99%	153
pelvis	99%	0.9	99%	48	99%	70	99%	4	98%	13	98%	145
humerus	86%	0.14	86%	86	95%	77	90%	18	91%	13	88%	198
radius	89%	0.14	80%	93	95%	78	91%	17	91%	15	90%	194
tibia	90%	0.13	84%	98	97%	85	97%	17	89%	14	89%	194
ulna	88%	0.18	86%	99	97%	75	95%	16	92%	6	85%	187
100%												
ribcage	99%	0.40	99%	50	99%	57	99%	5	99%	32	99%	153
pelvis	99%	0.8	99%	48	99%	68	99%	3	99%	14	98%	139
humerus	85%	0.12	80%	96	95%	84	87%	25	90%	11	87%	253
radius	89%	0.08	82%	103	98%	73	87%	20	90%	16	90%	231
tibia	90%	0.05	80%	98	97%	82	97%	25	94%	14	91%	256
ulna	87%	0.08	81%	99	97%	80	93%	18	90%	8	84%	254

Table 3. Mesh quality of corresponding target FEMs generated by different number of target feature points.

Data availability

The datasets used and analyzed during the current study available from the corresponding author on reasonable request.

Received: 2 February 2023; Accepted: 17 May 2023

Published online: 31 May 2023

References

- Zhou, B., Wang, X., Zhang, S., Li, Z. & Sun, Q. Comparing Factors Affecting Injury Severity of Passenger Car and Truck Drivers. *IEEE Access* **PP**, 1–1 (2020).
- Ma, Z., Mei, G. & Cuomo, S. An analytic framework using deep learning for the prediction of traffic accident injury severity based on contributing factors. *Accid. Anal. Prev.* **160**, 106322 (2021).
- Kumar, K. A. & Taj, Q. A study of pattern of injuries and factors affecting the injury pattern among road traffic accident victims. *Int. J. Commun. Med. Public Health* **7**, 1926 (2020).
- Ridella, S. A., Rupp, J. D. & Poland, K.
- Jiang, B. *et al.* Development of a 10-year-old paediatric thorax finite element model validated against cardiopulmonary resuscitation data. *Comput. Methods Biomech. Biomed. Eng.* **17**, 1185–1197 (2014).
- Nsiampa, N., Robbe, C. & Papy, A. Geometrical characteristics of a 50th anthropometric head finite element model: Literature review. *Hum Factors Mech. Eng. Def. Saf.* **6**, 1–16 (2022).
- Haug & Eberhard. Human Models for Crash and Impact Simulation. *Handbook of Numerical Analysis*, 231–452 (2004).
- Ruan, J., El-Jawahri, R., Chai, L., Barbat, S. & Prasad, P. Prediction and analysis of human thoracic impact responses and injuries in cadaver impacts using a full human body finite element model. *Stapp Car Crash J.* **47**, 299–321 (2003).
- Iwamoto, M., Kisanuki, Y., Watanabe, I., Furusu, K. & Hasegawa, J. Development of a finite element model of the total human model for safety (THUMS) and application to injury reconstruction. (2002).
- Gayzik, F. S., Moreno, D. P., Vavalle, N. A., Rhyne, A. C. & Stitzel, J. D. Development of a Full Human Body Finite Element Model for Blunt Injury Prediction Utilizing a Multi-Modality Medical Imaging Protocol. *intl Is* (2012).
- Shewchuk, J. R. Constrained Delaunay Tetrahedralizations and Provably Good Boundary Recovery. in *eleventh international meshing roundtable* (2002).
- Amezua, E., Hormaza, M. V., Hernández, A. & Ajuria, M. A method for the improvement of 3D solid finite-element meshes. *Adv. Eng. Softw.* **22**, 45–53 (1995).
- Roca, X., Sarrate, J. & Huerta, A. A new least-squares approximation of affine mappings for sweep algorithms. *Eng. Comput.* **26**, 327–337 (2010).
- Ledoux, F., Goff, N. L., Owen, S. J., Staten, M. L. & Weill, J. C. *A Constraint-Based System to Ensure the Preservation of Sharp Geometric Features in Hexahedral Meshes* (Springer, 2013).
- Vavalle, N. A., Schoell, S. L., Weaver, A. A., Stitzel, J. D. & Gayzik, F. S. Application of radial basis function methods in the development of a 95th percentile male seated FEA model. *Stapp Car Crash J.* **58**, 361 (2014).
- Schoell, S. L., Weaver, A. A., Urban, J. E., Jones, D. A. & Rupp, J. D. Development and validation of an older occupant finite element model of a mid-sized male for investigation of age-related injury risk. *Stapp Car Crash J.* **59**, 359 (2015).
- Kimpara, H., Lee, J. B., Yang, K. H., King, A. I. & Miki, K. Development of a Three-Dimensional Finite Element Chest Model for the 5(th) Percentile Female. *Stapp Car Crash Journal* (2005).

18. Dokko, Y., Ito, O. & Ohashi, K. Development of human lower limb and pelvis FE models for adult and the elderly. *SAE Technical Papers* (2009).
19. Mizuno, K., Iwata, K., Deguchi, T., Ikami, T. & Kubota, M. Development of a three-year-old child FE model. *Traffic Inj. Prev.* **6**, 361–371 (2005).
20. Yulong *et al.* A parametric ribcage geometry model accounting for variations among the adult population. *J. Biomech.* (2016).
21. Reed, *et al.* Development and validation of statistical models of femur geometry for use with parametric finite element models. *Ann. Biomed. Eng. J. Biomed. Eng. Soc.* **43**, 2503–2514 (2015).
22. Zhang, K. *et al.* An automated method to morph finite element whole-body human models with a wide range of stature and body shape for both men and women. *J. Biomech.* **60**, 253 (2017).
23. Feng, Z. *et al.* Computational modeling of traffic related thoracic injury of a 10-year-old child using subject-specific modeling technique. *Ann Biomed Eng* **44**, 258–271 (2016).
24. Wang, Y. *et al.* A parametric ribcage geometry model accounting for variations among the adult population. *J. Biomech.* **49**, 2791–2798 (2016).
25. Bellekens, B., Spruyt, V., Berkvens, R. & Weyn, M. in *Ambient: the Fourth International Conference on Ambient Computing*.
26. Myronenko, A. & Song, X. Point set registration: Coherent point drift. *IEEE Trans. Pattern Anal. Mach. Intell.* **32**, 2262–2275 (2010).
27. Donato, G. & Belongie, S. in *Proceedings of the 7th European Conference on Computer Vision-Part III*.

Acknowledgements

This work was supported financially by the Science and Technology Innovation Leading Talent of Hunan Province Project (2020RC4013), Natural Science Foundation Major Project of Hunan Province (2021JC0005), National Natural Science Foundation of China (U22A20187) and Science and Technology Innovation 2025 Major Project of Ningbo (2020Z033).

Author contributions

Q.Y. was responsible for the concept and design of the study and draft the manuscript. X.Z. and J.H. were responsible for data acquisition and analysis. Y.W. and C.C.C. revised it critically for important intellectual content. B.J. and S.X. completed the final approval of the submitted version.

Competing interests

The authors declare no competing interests.

Additional information

Correspondence and requests for materials should be addressed to B.J. or S.X.

Reprints and permissions information is available at www.nature.com/reprints.

Publisher's note Springer Nature remains neutral with regard to jurisdictional claims in published maps and institutional affiliations.



Open Access This article is licensed under a Creative Commons Attribution 4.0 International License, which permits use, sharing, adaptation, distribution and reproduction in any medium or format, as long as you give appropriate credit to the original author(s) and the source, provide a link to the Creative Commons licence, and indicate if changes were made. The images or other third party material in this article are included in the article's Creative Commons licence, unless indicated otherwise in a credit line to the material. If material is not included in the article's Creative Commons licence and your intended use is not permitted by statutory regulation or exceeds the permitted use, you will need to obtain permission directly from the copyright holder. To view a copy of this licence, visit <http://creativecommons.org/licenses/by/4.0/>.

© The Author(s) 2023